Sr–Si diagram at Si contents of 55–100 at.% and crystal structure of $SrSi_{2-x}$

Motoharu Imai[a]*, Kwangsik Han[b], Mitsuaki Nishio[c], Takeshi Kato[c], Satoshi Kawada[c], Satoshi Emura[b], Taichi Abe[b], Hiroshi Fujihisa[d]

[a] Research Center for Functional Materials, National Institute for Materials Science, Tsukuba, 305-0047, JAPAN

[b] Research Center for Structural Materials, National Institute for Materials Science, Tsukuba, 305-0047, JAPAN

[c] Research Network and Facility Service Division, National Institute for Materials Science, Tsukuba, 305-0047, JAPAN

[d] National Metrology Institute of Japan (NMIJ), National Institute of Advanced Industrial Science and Technology, Tsukuba, 305-8565, JAPAN

***Corresponding Author**
E-mail address: IMAI.Motoharu@nims.go.jp (M. Imai)
Phone Number: +81-29-859-2814

ORCID ID
M. Imai: 0000-0002-5848-113X
K. Han: 0000-0002-5701-5348
M. Nishio: 0000-0002-8177-3587
T. Kato: 0000-0002-3317-7481
S. Kawada: 0000-0003-4618-2746
S. Emura: 0000-0001-5789-6408
T. Abe: 0000-0002-5065-0939
H. Fijihisa: 0000-0001-9308-153X

Abstract

Cubic $SrSi_2$ has attracted attention as a thermoelectric material or Weyl semimetal candidate material. However, its physical properties have not been examined in detail. High-quality samples are required for this purpose. A previous study on the Sr–Si phase diagram reported that cubic $SrSi_2$ is a low-temperature phase and tetragonal $SrSi_2$ is a high-temperature phase based on little experimental evidence, highlighting the difficulty in synthesizing high-quality cubic $SrSi_2$ samples. Therefore, a new investigation of the Sr–Si phase diagram is necessary. This study experimentally investigated the Sr–Si diagram at Si contents of 55–100 at.% using arc-melted samples by performing inductively-coupled plasma optical emission spectroscopy, electron-probe microanalysis, powder X-ray diffraction analysis, and differential thermal analysis. Two intermetallic compounds ($SrSi_{2-x}$ and $SrSi_2$) and two eutectic reactions existed in this Si content range. The eutectic points were approximately 57 at.% and 1053.2 °C for Liquid ⇔ SrSi + $SrSi_{2-x}$ and approximately 75 at.% and 1050.0 °C for Liquid ⇔ $SrSi_2$ + Si. $SrSi_2$ had no high-temperature phase and melted congruently at 1121 °C. $SrSi_{2-x}$ existed at Si contents of 62.4–65.0 at.%, and it is formed by the peritectic reaction Liquid + $SrSi_2$ ⇔ $SrSi_{2-x}$. $SrSi_{2-x}$ crystallized into a monoclinic variant of the $\sqrt{5} \times \sqrt{5} \times 1$ α-$ThSi_2$-type superstructure with ordered Si defects at the body-center position of the cell (space group: *I*121, No. 5). $SrSi_{2-x}$ is the first example of the α-$ThSi_2$-type superstructure.

Keywords: silicides, phase diagrams, crystal structure, thermal analysis, X-ray diffraction, scanning electron microscopy SEM

1. Introduction

$SrSi_2$ has attracted considerable attention as a thermoelectric conversion material because of its relatively large dimensionless thermoelectric figure of merit (ZT = 0.15) at 300 K [1]. $SrSi_2$ crystallizes into a $SrSi_2$-type structure (cubic, space group $P4_132$, No. 213, or its enantiomer, $P4_332$, No. 212, Z = 4) [2,3]. It is considered to be a narrow-gap semiconductor [4] or Weyl semimetal candidate material [5,6]. However, its physical properties have not been investigated in detail. High-quality samples are required to examine physical properties, and a Sr–Si phase diagram is necessary for synthesizing high-quality samples.

The first Sr–Si phase diagram was constructed by Itkin and Alcock in 1989 [7] on the basis of the experimental data reported by Obinata et al. in 1965 [8]. This diagram included three intermetallic phases: Sr_2Si, SrSi, and $SrSi_2$. Two intermetallic compounds were discovered after 1964, i.e., Sr_5Si_3 with a Cr_5B_3-type structure (tetragonal, space group $I4/mcm$, No. 140, Z = 4) [9,10] and Sr_4Si_7 with a deficient α-$ThSi_2$-type structure (tetragonal, space group $I4_1/amd$, No. 141, Z = 4) [11]. Furthermore, cubic $SrSi_2$ transformed into a high-pressure (HP) phase with a tetragonal α-$ThSi_2$-type structure at HPs and high temperatures (HTs). Moreover, $SrSi_2$ with the α-$ThSi_2$ phase was quenched under ambient conditions [12-15]. A second phase diagram was constructed by Palenzona and Pani on the basis of their experimental work in 2004 [16]. Fig. 1 illustrates the Sr–Si phase diagram at Si contents of 50–100 at.% reported by Palenzona and Pani [16] and the experimental data reported by Rygalin et al. [17]. Palenzona and Pani claimed that $SrSi_2$ contained two phases: a room-temperature (RT) phase with a $SrSi_2$-type structure and an HT phase with an α-$ThSi_2$-type structure. They referred to the RT and HT phases as the α and β phases, respectively. Furthermore, they claimed that Sr_4Si_7 with a Si-deficient α-$ThSi_2$-type structure was the β phase of $SrSi_2$. These results were computationally examined by two groups [18,19].

The main problem in the report by Palenzona and Pani is that they did not observe the transformation from the $SrSi_2$-type structure to the α-$ThSi_2$-type structure (and vice versa). Instead, they used a transition temperature from the quenched α-$ThSi_2$ phase to the $SrSi_2$ phase at ambient pressure (400–450 °C for a HT X-ray diffraction (XRD) and 590–690 °C for differential thermal analysis (DTA)) [13] as the transition temperature for the RT-to-HT phase transition. We previously observed that the $SrSi_2$ phase is stable up to 600 °C in vacuum, 798 °C at 1.1 GPa, and 1098 °C at 3.0 GPa [15,20,21].

Rygalin et al. reported the “S-shaped” liquidus curve for Si contents of 78.5–100 at.% [17]. However, this must be reinvestigated because the shape of the liquidus curve was different from the generally expected shape.

For the aforementioned reasons, a reinvestigation of the Sr–Si phase diagram at Si-rich region is necessary.

In this study, we experimentally examined the Sr–Si phase diagram at Si contents of 55–100 at.% using inductively-coupled plasma optical emission spectroscopy (ICP-OES), electron-probe microanalysis (EPMA), powder XRD analysis, and DTA. We found two intermetallic compounds ($SrSi_{2-x}$ and $SrSi_2$) in this Si content range, contrary to the previously reported Sr–Si diagram. $SrSi_2$ had no high-temperature phase and it melted congruently at 1121 °C. $SrSi_{2-x}$ existed at Si contents of 62.4–65.0 at.%, and it is formed by the peritectic reaction Liquid + $SrSi_2 \Leftrightarrow SrSi_{2-x}$. $SrSi_{2-x}$ crystallized into a monoclinic variant of the $\sqrt{5} \times \sqrt{5} \times 1$ α-$ThSi_2$-type superstructure with ordered Si defects at the body-center position of the cell (space group: *I*121, No. 5). $SrSi_{2-x}$ is the first example of the α-$ThSi_2$-type superstructure. Furthermore, we found that the liquidus curve at Si contents higher than 75 at.% had a regular convex shape.

2. Experimental Methods

Samples were synthesized through the Ar-arc melting of (100-xs):xs molar mixtures of Sr (Aldrich, 4N) and Si (Furuuchi, 10N) ($45 \leq xs \leq 90$). Sr was weighed in an Ar-filled glove box (O_2 < 1 ppm, H_2O < 1 ppm). The chemical compositions of the starting materials are listed in Table 1. Several samples were annealed at 1030 °C for 72 h. Each sample was placed in a hexagonal BN (h-BN) capsule and sealed in an Ar-filled quartz tube. Then, they were annealed in an electrical furnace, and the quartz tubes were quenched in water.

The chemical compositions of the synthesized samples were determined by analyzing powdered samples using ICP-OES. ICP-OES was performed using an ICP-OES system (Agilent 720ES). The relative standard deviation (RSD) was estimated to be 1 wt.%, which corresponded to 0.66 at.% of Si for $SrSi_2$. The Cu concentration of arc-melted $SrSi_2$ was occasionally evaluated via ICP-OES; however, it was always below the detection limit (0.001 wt.%).

The chemical compositions of the phases observed in the samples were determined using EPMA with wavelength-dispersive X-ray spectroscopy (WDS). EPMA/WDS was performed using an electron-probe microanalyzer (JEOL, JXA 8500F) at an acceleration voltage of 15 kV and beam current of 50 nA. $SrAl_4$ and Si were used as standard materials. The chemical compositions were determined by averaging the compositions measured at five points. The RSD was estimated to be 3 wt.%.

The crystal structures of the samples were examined by performing powder XRD analysis using a Bragg–Brentano-type diffractometer (Rigaku, RINT-TTRIII) combined

with a high-speed one-dimensional detector (Rigaku, D/tex) with Cu Kα radiation (40 kV, 150 mA) and a step size of 0.02 for $2\theta = 5.00°–100.00°$. The powder XRD patterns of several samples were indexed using BIOVIA Materials Studio (MS) X-Cell (version 2022 HF1, Dassault Systémes) [22]. Rietveld analysis [23] was performed using MS Reflex (version 2022 HF1) [24].

Transformation temperatures were investigated using DTA. The samples (~20 mg) were placed in an h-BN capsule with an h-BN lid in an Ar-filled glovebox (O_2 < 1 ppm, H_2O < 1 ppm). The standard material (Al_2O_3) was also placed in the h-BN capsule with an h-BN lid. The sample and standard material were heated and cooled in a differential thermal analyzer (Rigaku, TG-DTA TG8120) at 10 K/min under Ar flow. The temperature was calibrated using the melting temperature of Au (1064.58 °C) [25].

For comparison, the quenched HP phase of $SrSi_2$ was synthesized by pressurizing and heating $SrSi_2$ with a $SrSi_2$-type structure at 5.5 GPa and 1100 °C using a belt-type HP apparatus [26].

3. Results and Discussion

3.1 Phase identification

Table 1 lists the nominal Si content, Si content observed using the ICP-OES analysis, microstructure constitutions, observed phases, and Si content of the observed phases determined by EPMA. The Si contents observed using the ICP-OES analysis were higher than the nominal Si content because Sr vaporizes during synthesis owing to its high vaporization pressure. Hereafter, the samples are indicated by the Si content determined via ICP-OES. Fig. 2 shows backscattered electron (BSE) images of several as-melted samples. The darker phase represents a higher Si content compared to the brighter phase because the atomic number of Si is smaller than that of Sr. The BSE images of the as-melted samples with other Si contents are shown in the Supplementary Data. The samples with 63.3 at.% Si and 66.1 at.% Si consist of a single phase (Figs. 2(d) and (f)). We refer to the phase that appears in the sample with 63.3 at.% Si as $SrSi_{2-x}$ because this phase exists at Si contents of 62.4–64.8 at.%, which includes the Si content of Sr_4Si_7 (63.6 at.%); this is discussed later. Powder XRD measurements show that the phase in the sample with 66.1 at.% Si is $SrSi_2$ with the $SrSi_2$-type structure; this is described later. The sample with 56.1 at.% Si has a hypoeutectic microstructure of SrSi and $SrSi_{2-x}$. SrSi (white needles in Fig. 2 (a)) is a primary phase. The sample with 57.8 at.% Si exhibits a lamellar structure. Considering the spatial resolution of WDS, measuring the chemical compositions of each phase that constructs the lamellar structure was difficult. The lamellar structure is generally formed by a eutectic reaction,

where the presumed eutectic reaction is Liquid ⇔ SrSi + $SrSi_{2-x}$. Because the size of both phases is small, the Si content for this eutectic reaction is deduced to be close to 57.8 %. A DTA curve of this sample has two transformation temperatures of 1053.0 and 1060.1 °C, as shown in Fig. 5 (a). Therefore, it is highly probable that this microstructure was formed by a hypereutectic reaction although the specific primary phase was difficult to find in the observed sight.

The sample with 59.6 at.% Si has a hypereutectic microstructure of SrSi and $SrSi_{2-x}$ with $SrSi_{2-x}$ primary phase (Fig. 2(c)). The sample with 64.4 at.% Si contains two phases, i.e., $SrSi_{2-x}$ and $SrSi_2$ (Fig. 2(e)). The sample with 68.1 at.% Si comprises a hypoeutectic microstructure of $SrSi_2$ and Si with a primary phase of $SrSi_2$ (Fig. 2(g)). The sample with 74.4 at.% Si exhibits a lamellar structure (Fig. 2(h)). Although the chemical composition of each phase with different contrast was not measured in the present study, the lamellar structure is deduced to be formed by the eutectic reaction of Liquid ⇔ $SrSi_2$ + Si, considering the results of EPMA and powder XRD analysis of the samples with 66.9–90.7 at.% Si. Because no noticeable primary phase was confirmed in the microstructure observations, the eutectic composition is deduced to be close to 74.4 at.% Si, which is consistent with that reported previously, 74 at.% Si [16]. The sample with 80.1 at.% Si contains a hypereutectic microstructure of $SrSi_2$ and Si with a primary phase of Si (Fig. 2(i)).

Table 1. Nominal Si content, Si content obtained in the ICP-OES analysis, microstructure constituents, observed phases, and Si contents of the observed phases determined by EPMA in (a) as-melted samples and (b) samples annealed in Ar atmosphere at 1030 °C for 72 h.

(a) As-melted samples

Nominal Si content (at%Si)	Observed Si content (at%Si)	Microstructure constitutions	Observed phases		Si content of observed phases	
			Phase 1	Phase 2	Phase 1 (at%Si)	Phase 2 (at%Si)
45.0	51.8	Primary phase + Eutectic 1 (E1)	SrSi		50.1	.
49.0	52.9				48.3	.
54.0	56.1				49.5	
56.0	57.8	Eutectic 1(E1)				
58.0	59.6	Primary phase + Eutectic 1(E1)	$SrSi_{2-x}$		62.4	
60.0	60.8				62.7	
62.0	62.6	Single phase			63.0	
62.0	63.3				64.5	
63.0	63.8				64.8	
64.0	64.4	Two phases	$SrSi_{2-x}$	$SrSi_2$	64.6	67.1
64.0	64.8				64.8	67.3
65.0	65.5				64.5	67.1
66.0	66.1	Single Phase	$SrSi_2$		67.0	
67.0	66.9	Primary phase +Eutectic 2 (E2)			66.6	
68.0	68.1				66.7	
70.4	70.5				67.0	
72.5	72.4				66.9	
74.6	74.4	Eutectic 2*				
75.8	75.3					
80.0	80.1	Primary phase + Eutectic 2 (E2)	Si			
83.5	84.0					
90.0	90.7					

(b) Annealed samples

Nominal Si content (at%Si)	Observed Si content (at%Si)	Microstructure constitutions	Observed phases		Si content of observed phases	
			Phase 1	Phase 2	Phase 1 (at%Si)	Phase 2 (at%Si)
63.0	63.8	Single phase	$SrSi_{2-x}$	-	64.7	-
64.0	64.4	Two phases of phase 1 and phase 2	$SrSi_{2-x}$	$SrSi_2$	65.0	67.2
65.0	65.7				64.4	67.1
66.0	65.9	Single phase	$SrSi_2$	-	67.2	-
67.0	67.5	Two phases of phase 1 and phase 2	$SrSi_2$	Si	66.7	
68.0	68.1				66.9	

E1: Lamellar structure of $SrSi_{2-x}$ and $SrSi_2$. E2: Lamellar structure of $SrSi_2$ and Si.
*: Undefined whether hypoeutectic or hypereutectic.

Several samples with nominal Si content of 60.0–68.0 at.% Si listed in Table 1 (a) were annealed at 1030 °C for 72 hours to investigate the relation among SrSi, $SrSi_{2-x}$, $SrSi_2$, and Si in detail. The annealing slightly changes the Si contents of samples, as shown in Table 1 (b). Fig. 3 is BES images of annealed samples. The sample with 63.8 at.% Si consists of a single $SrSi_{2-x}$ phase (Fig. 3(a)). The sample with 64.4 at.% Si consists of two phases, i.e., $SrSi_{2-x}$ and $SrSi_2$ (Fig. 3(b)). The sample with 65.9 at.% Si consists of a single $SrSi_2$ phase (Fig. 3(c)). The sample with 67.5 at.% Si consists of two phases, i.e., $SrSi_2$ and Si (Fig. 3(d)).

We examined the microstructure of the sample with 64.4 at.% Si by measuring the line profile using EPMA/WDS (Fig. 3(e)). The dark and bright gray areas contain approximately 67 at.% Si and 64 at.% Si, respectively, which correspond to the Si contents of $SrSi_2$ and $SrSi_{2-x}$, respectively. Thus, the sample with 64.4 at.% Si consists of $SrSi_2$ and $SrSi_{2-x}$, and it does not contain a eutectic microstructure.

Figure 4 presents the powder XRD patterns of the as-melted samples and the XRD patterns of SrSi, Sr_4Si_7, and $SrSi_2$ simulated using the crystallographic data provided in previous works [3,11,27]. The peaks observed for the sample with 56.1 at.% Si can be assigned to SrSi and Sr_4Si_7. The main peaks for the sample with 63.3 at.% Si can be assigned to Sr_4Si_7. However, this sample shows low-intensity peaks at 2θ = 10.98° and 17.98° (indicated by asterisks), which cannot be assigned to Sr_4Si_7. This is

discussed later. The peaks for the sample with 64.6 at.% Si can be assigned to Sr_4Si_7 and $SrSi_2$. The peaks for the sample with 66.2 at.% Si can be assigned to $SrSi_2$. The sample with 75.3 at.% Si shows the peak for Si in addition to the peaks for $SrSi_2$.

The chemical compositions and phases observed in the samples are summarized in Table 1. SrSi, $SrSi_{2-x}$, $SrSi_2$, and Si exist at Si contents of 51.8–90.7 at.%. SrSi has Si contents of 48.3–50.1 at.%. $SrSi_{2-x}$ has Si contents of 62.4–64.8 at.%, which include the Si content of Sr_4Si_7 (63.6 at.%). Moreover, $SrSi_2$ has Si contents of 66.1–67.3 at.%. The Sr content in the Si phase of the arc-melted samples with 80.1–90.7 at.% Si was under our detection limited (0.01 at.%). The Sr contents of the Si phase of the annealed samples with 67.5 and 68.1 at.% Si were approximately 0.2 at.% Si, which is lower than the Sr solid solution limit reported in Ref. 17 (1.15 at.%).

3.2 Liquidus temperature and invariant reactions

3.2.1 Si contents of 56–63 at.%

Figure 5(a) shows the DTA curves for the samples with 56.1–62.6 at.% Si. The temperatures for the phase transition and eutectic reaction were determined from the onset of endothermic reactions and the liquidus temperatures were obtained from the peak of the curves, as shown by arrows in the figure. These temperatures were determined from the intersection point of two fitted lines, as shown by the dashed lines in the figure. The transformation temperatures are summarized in Table 2.

Figure 5(b) shows the phase diagram at Si contents of 56–63 at.% constructed using the results of the DTA, powder XRD measurements, and EPMA. We determined the eutectic point for the reaction (SrSi + $SrSi_{2-x}$ $\Leftrightarrow$ Liquid) to be approximately 57 at.% and 1053.2 °C on the basis of the DTA curves shown in Fig. 5(a) and the BSE images shown in Figs. 2(a)–(c). A previous study reported the eutectic reaction (SrSi + $SrSi_2$ $\Leftrightarrow$ Liquid) at approximately 61 at.% Si and 1055 °C [16]. The eutectic composition for the reaction observed in the present study is different from that reported in the previous study although the temperatures were almost identical. We attribute this discrepancy to the fact that the eutectic composition was determined based on the small amount of DTA data without the observation of the microstructure in Ref. 16.

Unidentified endothermic reactions are observed at 1032.2 °C at Si contents of 56.1–60.8 at.%, as suggested in the previous study [16].

Table 2. Transformation temperatures determined by DTA measurements.

Si content determined by ICP-OES (at. %)	56.1	57.8	59.6	60.8	62.6	63.3	63.5	63.8	64.4	64.4	64.8	Average			
Anneal (Y/N)	N	N	N	N	N	N	Y	N	N	Y	N				
Transformation Temperature (°C)															
Liquidus	-	1060.1	1097.7	1104.6	1110.5	1112.3	1113.8	1112.8	1120.7	1119.8	1119.6				
$SrSi_{2-x}$ ⇔ L + $SrSi_2$							1106.5		1105.9	1106.2	1105.7	1106.1			
SrSi + $SrSi_{2-x}$ ⇔ L	1053.9	1053.0	1052.0	1053.8								1053.2			
Unidentified	1030.3	1029.6	1029.6	1039.1								1032.2			
Si content determined by ICP-OES (at. %)	65.5	65.7	65.9	66.1	66.2	68.1	70.5	72.4	74.4	75.3	78.1	80.1	84	90.7	Average
Anneal (Y/N)	N	Y	Y	N	N	N	N	N	N	N	N	N	Y	Y	
Transform Temperature (°C)															
Liquidus	1120.0	1121.1	1121.4	1118.3	1118.4	1108.6	1089.1	-	-	-	1157.4	1207.6	1270.2	1338.6	
$SrSi_2$ + Si ⇔ L				1048.7	1049.2	1049.9	1049.2	1049.3	1050.6	1050.8	1050.3	1051.1	1050.7	1050.3	1050.0

3.2.2 Si contents of 63–67 at.%

As shown in Fig. 6(a), no endothermic reaction is observed at temperatures of 100–900 °C for the samples with Si contents of 65.6–68.1 at.%. This indicates that $SrSi_2$ does not undergo the RT-to-HT phase transition.

Figure 6(b) shows the DTA curves for the annealed samples with 63.5–65.9 at.% Si. The DTA curves for the as-melted samples are provided in the Supplementary Data. Figure 6(c) shows the phase diagram at Si contents of 60–70 at.% constructed using the DTA curves, powder XRD patterns, and BSE images. Two intermetallic compounds—$SrSi_{2-x}$ and $SrSi_2$—exist in this Si content range. $SrSi_{2-x}$ exists approximately between 62 and 64 at.% Si, and it is formed by the peritectic reaction Liquid + $SrSi_2 \Leftrightarrow SrSi_{2-x}$. $SrSi_2$ has no HT phase and it melts congruently at 1121.4 °C. The difference between the liquidus temperature and peritectic temperature is less than 13.6 K. Moreover, the composition-temperature area for L+$SrSi_2$ is small.

The above results are contrary to the previously reported phase diagram, in which only $SrSi_2$ exists in this Si content range and $SrSi_2$ contains the low-temperature and HT phases [16]. The previously reported transformation temperatures [16] (indicated by empty squares) are consistent with the phase diagram obtained in this study. Thus, the discrepancies between the phase diagrams obtained in this work and the previous study [16] may be due to the small number of data points used in the previous study.

We observed a single $SrSi_{2-x}$ phase in the as-melted sample with 63.3 at.% Si (Fig. 2 (d)). However, two phases, $SrSi_{2-x}$ and $SrSi_2$, are expected to be observed in the case that $SrSi_{2-x}$ is formed by the peritectic reaction $SrSi_{2-x} \Leftrightarrow$ L + $SrSi_2$, as shown in the as-melted sample with 64.4 at.% Si (Fig. 2 (e)). At 63.3 at. % Si, the difference between the transformation temperature for this peritectic reaction and the liquidus temperature is considerably small, that is, 4.8 K. Furthermore, the amount of the precipitated $SrSi_2$ phase is expected to be small at 63.3 at. % Si by the lever rule, and the cooling rate of the arc-melting furnace is high. Therefore, we believe that we observed the single $SrSi_{2-x}$ phase in this as-melted sample by a combination of these three factors.

3.2.3 Si contents higher than 67 at.%

Figures 7(a) and (b) show the DTA curves for the samples with 68.1–90.7 at.% Si. Figure 7(c) shows the phase diagram at Si contents of 70–100 at.% constructed using the DTA curves, powder XRD patterns, and BSE images. The melting temperature of Si (1414 °C) is taken from literature [28]. The eutectic point for the invariant reaction ($SrSi_2$ + Si $\Leftrightarrow$ Liquid) is approximately 75 at.% and 1050.0 °C, which is consistent with previous results [16] (approximately 75 at.% and 1045 °C). The liquidus curve at Si contents higher than 75 at.% is convex, which is in contrast to the results reported in

literature [17].

3.3 Phase diagram

Figure 8 shows the binary Sr–Si diagram at Si contents of 55–100 at.%. Two intermetallic compounds—$SrSi_{2-x}$ and $SrSi_2$—exist in this Si content range. $SrSi_{2-x}$ exists approximately between 62 and 64 at.% Si, and it is formed by the peritectic reaction Liquid + $SrSi_2$ ⇔ $SrSi_{2-x}$. $SrSi_2$ has no HT phase, and it melts congruently at 1121.4 °C. The eutectic point for the reaction (SrSi + $SrSi_{2-x}$ ⇔ Liquid) is approximately 57 at.% and 1053.2 °C. The eutectic composition for this reaction is different from that for the reaction (SrSi + $SrSi_{2-x}$ ⇔ Liquid) reported in a previous study [16]. The eutectic point for the invariant reaction ($SrSi_2$ + Si ⇔ Liquid) is approximately 75 at.% and 1050.0 °C, which is the almost the same as that reported in the previous study [16]. The liquidus curve at Si contents higher than 75 at.% has a regular convex shape.

This phase diagram indicates that a high-quality sample of $SrSi_2$ with the $SrSi_2$-type structure can be synthesized by melting and solidifying $SrSi_2$. As the Si content of $SrSi_2$ is close to that of $SrSi_{2-x}$, $SrSi_{2-x}$ may be included in the $SrSi_2$ samples synthesized via the simple melting and solidification of $SrSi_2$. In this case, the vertical Bridgeman method or floating-zone method are expected to be effective for growing high-quality $SrSi_2$ samples without $SrSi_{2-x}$.

3.4 Crystal structure of $SrSi_{2-x}$

Figure 9 shows the powder XRD patterns of $SrSi_{2-x}$ and the quenched HP phase of $SrSi_2$, i.e., α-$ThSi_2$-phase $SrSi_2$. The XRD pattern of the quenched HP phase of $SrSi_2$ agrees well with simulated pattern of α-$ThSi_2$-phase $SrSi_2$ [12]. The high-intensity peaks in the XRD pattern of $SrSi_{2-x}$ agree with those in the simulated pattern of Sr_4Si_7 [11], which consists of the α-$ThSi_2$-type structure with disordered Si vacancies. The simulated XRD pattern of Sr_4Si_7 shows only the peaks of α-$ThSi_2$-phase $SrSi_2$ because disordered Si vacancies exist in the Si-deficient α-$ThSi_2$-type structure. However, the powder XRD pattern of $SrSi_{2-x}$ contains three additional low-intensity peaks, as indicated by the asterisks in the figure. The peaks at 2θ = 10.98° and 17.98° (d values = 8.058 Å and 4.934 Å) are consistent with reports that powder XRD patterns contain two extra lines at low angles (d values = 8.025 Å and 4.910 Å) [16]. Thus, the crystal structure of $SrSi_{2-x}$ is different from the α-$ThSi_2$-structure with disordered Si vacancies. These small peaks cannot be assigned to the α-$ThSi_2$-type superstructure proposed by Nentwich et al., which is a $\sqrt{2} \times \sqrt{2} \times 1$ tetragonal variant of the α-$ThSi_2$-type structure [29].

Figure 10 shows the powder XRD pattern for $SrSi_{2-x}$ and the results of the

Rietveld analysis [23]. In the final stage of analysis, the structure is optimized using the "Rietveld with energies" mode in Reflex [24] with the COMPASS III force field [30]. The observed pattern is accurately reproduced by assuming that $SrSi_{2-x}$ has a monoclinic structure, as shown in Table 3.

Table. 3. Crystal structure of $SrSi_{2-x}$. Monoclinic. Space group: *I*2 (*I* 1 2 1) (No. 5, unique axis *b*, cell choice 3). Lattice parameters: $a = 9.8722 \pm 0.0004$ Å, $b = 13.8971 \pm 0.0005$ Å, $c = 9.8750 \pm 0.0004$ Å, $\alpha = \gamma = 90.000°$, $b = 90.344 \pm 0.002°$, $V = 1354.8$ Å^3. $Z = 2$. $U_{iso} = 0.029 \pm 0.001$ Å^2. The occupancy of each atom is 1. Chemical formula: $Sr_{10}Si_{19}$. R factors: $R_{wp} = 10.70\%$, $R_p = 20.91\%$, $R_e = 6.85\%$, $S = 1.56$. The definitions of R_{wp}, R_p, R_e, and S are provided in literature [23].

Label	Atom	Multiplicity, Wycoff Letter	*x*	*y*	*z*
Sr1	Sr	4c	0.20095	0.64685	0.90319
Sr2	Sr	4c	0.9032	-0.09317	0.29203
Sr3	Sr	4c	0.29192	-0.10286	0.09846
Sr4	Sr	4c	0.59837	0.65432	0.69682
Sr5	Sr	2b	0	0.64945	0.5
Sr6	Sr	2a	0.5	-0.1139	0.5
Si1	Si	4c	0.2446	0.07717	0.87824
Si2	Si	4c	0.61586	0.06251	0.69804
Si3	Si	4c	0.90029	0.31843	0.30107
Si4	Si	4c	0.69199	0.31571	0.90313
Si5	Si	4c	0.30856	0.48269	0.09945
Si6	Si	4c	0.92327	0.48421	0.28965
Si7	Si	4c	0.60106	0.22721	0.70337
Si8	Si	4c	0.77918	0.24057	0.11158
Si9	Si	2b	0	0.06759	0.5
Si10	Si	2b	0	0.23582	0.5
Si11	Si	2a	0.5	0.29748	0.5

Figures 11 (a)–(d) show the crystal structure of $SrSi_{2-x}$. The lattice parameter *a* is approximately equal to the lattice parameter *c*. The angle β is 90.344º, which is slightly deviated from 90.00º, whereas the other two angles are 90.00º. $SrSi_{2-x}$ contains two Si vacancies in the unit cell, which occupy the 2a site (0, 0, 0), as indicated by the red spheres in Fig. 11(d). The chemical formula for this structure is $Sr_{10}Si_{19}$, which

corresponds to a Si content of 65.5 at.%. This agrees with the Si content of $SrSi_{2-x}$ in the annealed samples (64.4–65.0 at.%) determined via EPMA/WDS within experimental error.

The crystal structure of $SrSi_{2-x}$ can be related to that of the α-$ThSi_2$-type $SrSi_2$ shown in Figs. 11 (e)–(h). The comparison between Figs. 11 (b) and (f) shows that the lattice parameter *a* of $SrSi_{2-x}$ is approximately the same as √5 times the lattice parameter *a* of α-$ThSi_2$-type $SrSi_2$. The comparison between Figs. 11 (d) and (h) shows that the crystal structure of $SrSi_{2-x}$ is closely related to that of the α-$ThSi_2$-type $SrSi_2$ although $SrSi_{2-x}$ has vacancies. Thus, the crystal structure of $SrSi_{2-x}$ is a monoclinic variant of √5 × √5 × 1 α-$ThSi_2$-type superstructure with ordered Si defects. This $Sr_{10}Si_{19}$-type structure is the first observed α-$ThSi_2$-type superstructure.

The Si net in $SrSi_{2-x}$ is slightly deformed compared with that in α-$ThSi_2$-phase $SrSi_2$. The Si–Si bond-length deviations from the α-$ThSi_2$-type structure are less than 6%. The three Si–Si–Si bond angles around defects (orange sections in Fig. 11 (d)) are larger than the corresponding angles in the α-$ThSi_2$-type structure by several degrees. This may be because the Si atom at the vertex is pulled from the two neighboring Si atoms.

4. Conclusions

The Sr–Si diagram is experimentally investigated at Si contents of 55–100 at.% using as-melted and annealed samples by utilizing ICP-OES, EPMA, powder XRD, and DTA. Two intermetallic compounds exist in this Si content range, i.e., $SrSi_{2-x}$ and $SrSi_2$. $SrSi_{2-x}$ exists approximately between 62 and 64 at.% Si, and it is formed by the peritectic reaction Liquid + $SrSi_2$ ⇔ $SrSi_{2-x}$. $SrSi_2$ has no HT phase and it melts congruently at 1121.4 °C. $SrSi_{2-x}$ crystalizes into a monoclinic variant of the √5 × √5 × 1 α-$ThSi_2$-type superstructure with ordered Si defects at the body-center position of the cell (space group: *I*121, No. 5).

The phase diagram constructed in this study indicates that high-quality samples of $SrSi_2$ with the $SrSi_2$-type structure can be synthesized using the vertical Bridgeman method or floating-zone method. This can help in growing high-quality single crystals of $SrSi_2$, which are required for a detailed examination of the physical properties of $SrSi_2$.

Acknowledgments

The authors thank Akira Ishitoya of National Institute for Materials Science (NIMS) for chemical-composition analysis using ICP-OES, Masahiko Kawasaki of NIMS for sealing the samples in quartz tubes, Megumi Sato of NIMS for her experimental support, and

Takashi Taniguchi of NIMS for allowing us to use the belt-type high-pressure apparatus. This study was partially supported by a Grant-in-Aid for Scientific Research (KAKENHI) (grant number JP22H00268) from the Japan Society for the Promotion of Science (JSPS) and a Grant-in-Aid from Iketani Science and Technology Foundation (grant number 0341201-A).

Supplementary Data

BSE images of arc-melted samples and DTA curves of arc-melted samples with 63.3–66.1 at. % Si on heating. This material is available free of charge online at *.

References

[1] S.K. Singh, M. Imai, Thermoelectric properties of cubic Ba-substituted strontium disilicide, $Sr_{1-x}Ba_xSi_2$, with Ba content above solid solubility limit, Intermetallics. 127 (2020) 106981. https://doi.org/10.1016/j.intermet.2020.106981.

[2] K. Janzon, H. Schäfer, A. Weiss, Crystal structure of strontium disilicide, Angew. Chem. Int. Ed. Engl. 4 (1965) 245. https://doi.org/10.1002/anie.196502452.

[3] G.E. Pringle, The structure of $SrSi_2$: a crystal of class O (432), Acta Crystallogr. B Struct. Sci. 28 (1972) 2326–2328. https://doi.org/10.1107/S0567740872006053.

[4] M. Imai, T. Naka, T. Furubayashi, H. Abe, T. Nakama, K. Yagasaki, Electrical properties of polycrystalline $SrSi_2$, Appl. Phys. Lett. 86 (2005) 032102. https://doi.org/10.1063/1.1849423.

[5] S.M. Huang, S.Y. Xu, I. Belopolski, C.C. Lee, G. Chang, T.R. Chang, B. Wang, N. Alidoust, G. Bian, M. Neupane, D. Sanchez, H. Zheng, H.T. Jeng, A. Bansil, T. Neupert, H. Lin, M.Z. Hasan, New type of Weyl semimetal with quadratic double Weyl fermions, Proc. Natl Acad. Sci. U. S. A. 113 (2016) 1180–1185. https://doi.org/10.1073/pnas.1514581113.

[6] B. Singh, G.Q. Chang, T.R. Chang, S.M. Huang, C.L. Su, M.C. Lin, H. Lin, A. Bansil, Tunable double-Weyl Fermion semimetal state in the $SrSi_2$ materials class, Sci. Rep. 8 (2018) 10540. https://doi.org/10.1038/s41598-018-28644-y.

[7] V.P. Itkin, C.B. Alcock, The Si-Sr (silicon-strontium) system, Bull. Alloy Phase Diagrams. 10 (1989) 630–634. https://doi.org/10.1007/BF02877630.

[8] I. Obinata, Y. Takeuchi, K. Kurihara, M. Watanabe, Über die Legierungen des mangans und Siliziums mit alkali-und Erdalkalimetallen, Metall. 19 (1965) 21–35.

[9] G. Nagorsen, G. Rocktäschel, H. Schäfer, A. Weiss, Die Kristallstruktur der phase Sr_5Si_3, Z. Naturforsch. B. 22 (1967) 101–102. https://doi.org/10.1515/znb-1967-0122.

[10] R. Nesper, F. Zürcher, Redetermination of the crystal structure of pentastrontium trisilicide, Sr_5Si_3, Z. Kristallogr. New Cryst. Struct. 214 (1999) 19. https://doi.org/10.1515/ncrs-1999-0112.

[11] K.H. Janzon, H. Schäfer, A. Weiss, Sr, Si_7, eine neue phase in system Sr-Si, Z. Naturforsch. B. 22b (1967) 100–101.

[12] J. Evers, G. Oehlinger, A. Weiss, Effect of pressure on the structures of divalent metal disilicides MSi_2 (M=Ca,Eu,Sr), J. Solid State Chem. 20 (1977) 173–181. https://doi.org/10.1016/0022-4596(77)90065-2.

[13] J. Evers, Transformation of 3-dimensional 3-connected silicon nets in $SrSi_2$, J. Solid State Chem. 24 (1978) 199–207. https://doi.org/10.1016/0022-4596(78)90010-5.

[14] J. Evers, Phase diagram of $SrSi_2$ to 40 kbar and 1200 °C, J. Phys. Chem. Solids. 40 (1979) 951–954. https://doi.org/10.1016/0022-3697(79)90123-9.

[15] M. Imai, T. Kikegawa, Phase transitions of alkaline-earth-metal disilicides $M_{AE}Si_2$ (M_{AE} = Ca, Sr, and Ba) at high pressures and high temperatures, Chem. Mater. 15 (2003) 2543–2551. https://doi.org/10.1021/cm0207954.

[16] A. Palenzona, M. Pani, The phase diagram of the Sr–Si system, J. Alloys Compd. 373 (2004) 214–219. https://doi.org/10.1016/j.jallcom.2003.11.003.

[17] B. Rygalin, V. Prokofieva, L. Pavlova, Y.E. Sokolov, The Si–Sr and Si–Ba phase diagrams over the Si-rich composition range, Calphad. 34 (2010) 196–199. https://doi.org/10.1016/j.calphad.2010.02.005.

[18] A. Garay, G. Trápaga, Z.K. Liu, R. Arróyave, Thermodynamic modeling of the Si–Sr system, Calphad. 33 (2009) 550–556. https://doi.org/10.1016/j.calphad.2009.07.001.

[19] K. Li, S.H. Liu, C.S. Sha, Y. Du, A thermodynamic reassessment of the Si–Sr system, Calphad. 35 (2011) 594–600. https://doi.org/10.1016/j.calphad.2011.09.007.

[20] M. Imai, T. Hirano, T. Kikegawa, O. Shimomura, Phase transitions of $BaSi_2$ at high pressures and high temperatures, Phys. Rev. B. 58 (1998) 11922–11926. https://doi.org/10.1103/PhysRevB.58.11922.

[21] M. Imai, Thermal expansion of alkaline-earth-metal disilicides $AeSi_2$ (Ae = Ca, Sr, and Ba), Jpn. J. Appl. Phys. 50 (2011) 101801. https://doi.org/10.1143/JJAP.50.101801.

[22] M.A. Neumann, X-cell: a novel indexing algorithm for routine tasks and difficult cases, J. Appl. Crystallogr. 36 (2003) 356–365. https://doi.org/10.1107/S0021889802023348.

[23] R.A. Young, The Rietveld Method, Oxford University Press, New York, 1995.

[24] Dassault Systéms Americas Corp., BIOVIA Materials Studio Reflex website, 2023. https://www.3ds.com/products-services/biovia/products/molecular-modeling-simulation/biovia-materials-studio/battery-materials/. (accessed January 25).
[25] J. Emsley, The Elements, third ed, Clarendon Press, Oxford, 1998.
[26] S. Yamaoka, M. Akashi, H. Kanda, T. Osawa, T. Taniguchi, H. Sei, O. Fukunaga, Development of belt type high pressure apparatus for material synthesis at ~8 GPa, J. High Press. Inst. Jpn. 30 (1992) 249–258.
[27] A. Currao, J. Curda, R. Nesper, Can one design Zintl anions? Contributions from the system Sr/Mg/Si to the topic Si_2, Z. Anorg. Allg. Chem. 622 (1996) 85–94. https://doi.org/10.1002/zaac.19966220113.
[28] R. Hull, Properties of Crystalline Silicon, Inspec, London, 1999.
[29] M. Nentwich, M. Zschornak, M. Sonntag, R. Gumeniuk, S. Gemming, T. Leisegang, D.C. Meyer, Structure variations within RSi_2 and R_2TSi_3 silicides. Part I. Structure overview, Acta Crystallogr. B Struct. Sci. Cryst. Eng. Mater. 76 (2020) 177–200. https://doi.org/10.1107/S2052520620001043.
[30] R.L.C. Akkermans, N.A. Spenley, S.H. Robertson, COMPASS III: Automated fitting workflows and extension to ionic liquids, Mol. Simul. 47 (2021) 540–551. https://doi.org/10.1080/08927022.2020.1808215.

Figure Captions

Fig. 1. Previously reported Sr–Si phase diagram at Si contents of 50–100 at.% [16,17].

Fig. 2 BSE images of as-melted samples with Si contents of (a) 56.1 at.%, (b) 57.8 at.%, (c) 59.6 at.%, (d) 63.3 at.%, (e) 64.4 at.%, (f) 66.1 at.%, (g) 68.1 at.%, (h) 74.4 at.%, and (i) 80.1 at.%.

Fig. 3 BSE images of annealed samples with Si contents of (a) 63.8 at.%, (b) 64.4 at.%, (c) 65.9 at.%, and (d) 68.1 at.%. (e) Composition profile measured along the white line for the 64.4 at.% Si sample.

Fig. 4. Powder XRD patterns of as-melted samples and simulated patterns of SrSi, Sr_4Si_7, and $SrSi_2$ [3,11,27].

Fig. 5. (a) DTA curves of samples with Si contents of 56.1–62.6 at.%. The arrows indicate transformation temperatures. (b) Phase diagram at Si contents of 56–63 at.%. The colors of solid rhombuses correspond to the colors of DTA curves in (a). The empty squares, gray solid and dashed lines are representative of the data reported by Palenzona and Pani [16].

Fig. 6. (a) DTA curves of as-melted samples with Si contents of 65.6 at.%, 66.1 at.%, and 68.1 at.%. The arrows indicate transformation temperatures. (b) DTA curves of annealed samples with Si contents of 63.5–65.9 at.%. (c) Phase diagram at Si contents of 60–70 at.%. The colors of solid rhombuses correspond to the colors of DTA curves in (b). The solid circles and triangles represent the Si content at which the samples annealed at 1030 °C contain a single phase and two phases, respectively. The empty squares, gray solid lines, and dashed lines represent the data reported by Palenzona and Pani [16].

Fig. 7. (a) DTA curves of as-melted samples with Si contents of 68.1–74.4 at.%. The arrows indicate transformation temperatures. (b) DTA curves of samples with Si contents of 78.1–90.7 at.%. (c) Phase diagram at Si contents of 70–100 at.%. The colors of solid rhombuses correspond to the colors of DTA curves in (a) and (b). The data reported by Palenzona and Pani [16] and Rygalin et al. [17] are also plotted.

Fig. 8. Sr–Si phase diagram at Si contents of 55–100 at.%.

Fig. 9. Powder XRD patterns of $SrSi_{2-x}$ and the quenched HP phase of $SrSi_2$ and simulated XRD patterns of Sr_4Si_7 [11] and α-$ThSi_2$-phase $SrSi_2$ [12].

Fig. 10. Powder XRD patterns of $SrSi_{2-x}$. The red points and blue line represent observed and calculated intensities (I_{obs} and I_{cal}) of $Sr_{10}Si_{19}$, respectively. Peak positions for $Sr_{10}Si_{19}$ are labeled by green vertical bars located at −10000 counts. The difference between the two intensities (I_{obs} - I_{cal}) is indicated by the black line shifted by −20000 counts.

Fig. 11. Crystal structures of (a–d) $SrSi_{2-x}$. and (e–h) α-$ThSi_2$-phase $SrSi_2$. (a) General view, (b) view along the [010] direction, (c) view along the [001] direction, and (d) view along the [001] direction rotated slightly around the *a* axis. (e) General view, (f) view along the [001] direction, (g) view along the [010] direction, and (h) view of 2 × 2 × 1 super cell along the direction where the *b* axis is rotated by 26.5° degree around the c axis and slightly tilted around the *b* axis. The cell is shifted along the [001] direction. The large green and small blue spheres represent Sr and Si atoms, respectively. Red spheres in (d) represent Si vacancies. Red bonds are added to show the relationship between α-$ThSi_2$-phase $SrSi_2$ and $Sr_{10}Si_{19}$.

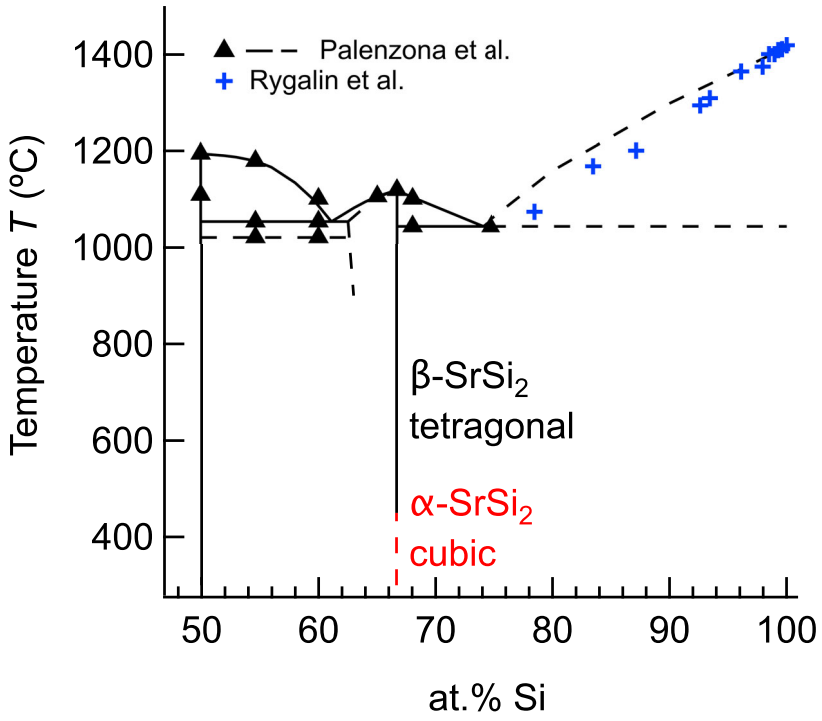
Palenzona et al.
Rygalin et al.
Temperature T (°C)
1400
1200
1000
800
600
400
50
60
70
80
90
100
at.% Si
β-SrSi2
tetragonal
α-SrSi2
cubic

Fig. 1.

(a) 56.1 at. % Si

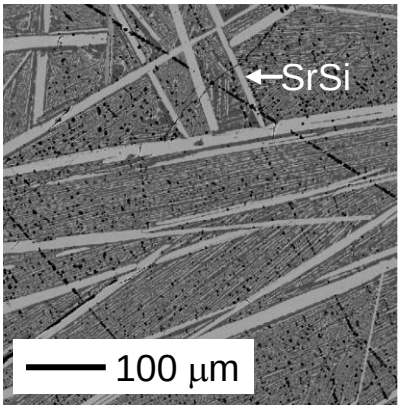

(b) 57.8 at. %

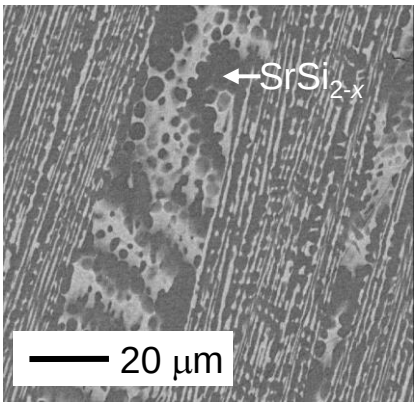

(c) 59.6 at. %

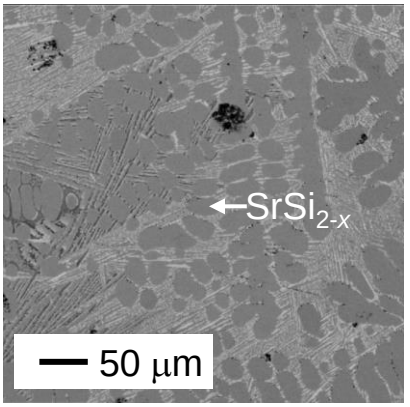

(d) 63.3 at. %

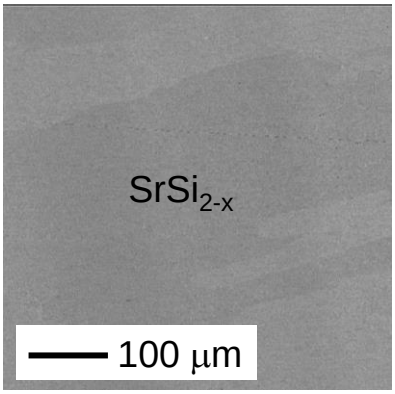

(e) 64.4 at.%

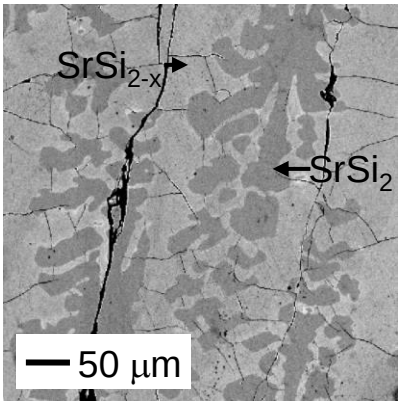

(f) 66.1 at.%

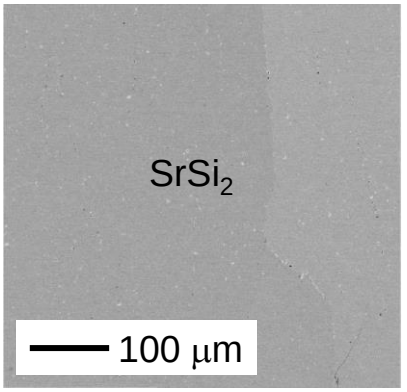

(g) 68.1 at.%

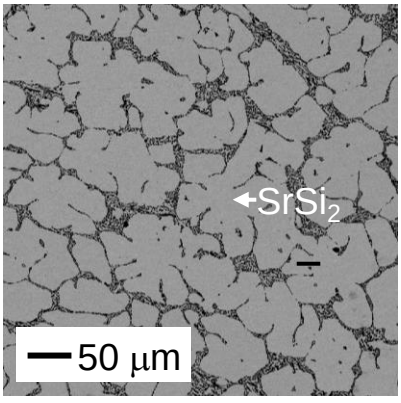

(h) 74.4 at.%

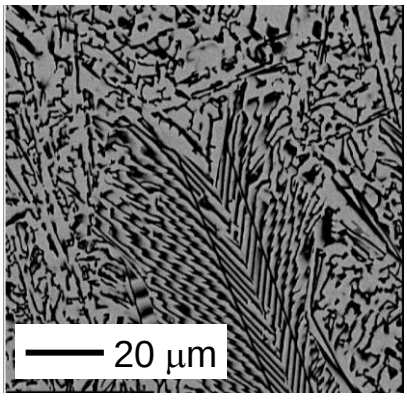

(i) 80.1 at. %

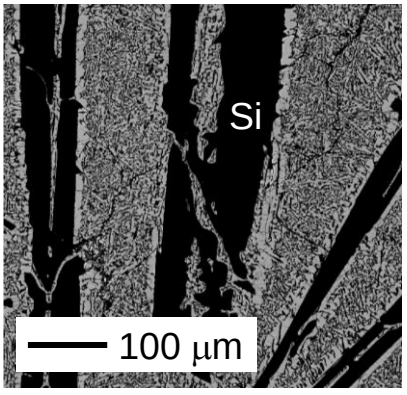

Fig. 2

(a) 63.8 at. %

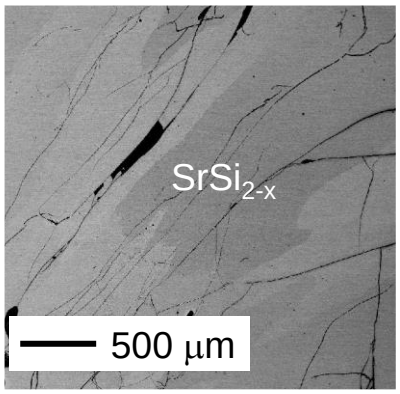

(b) 64.4 at. %

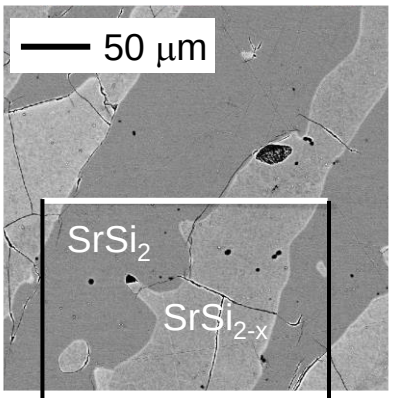

(c) 65.9 at. %

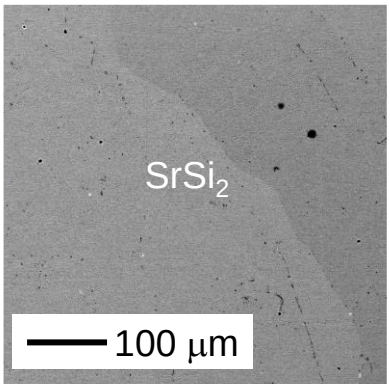

(d) 67.5 at. %

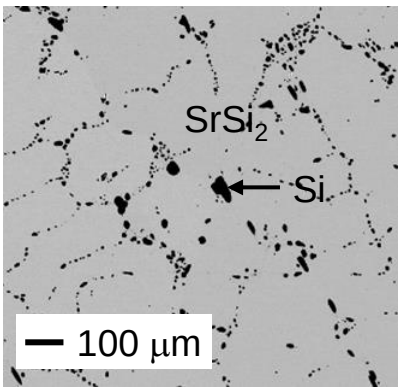

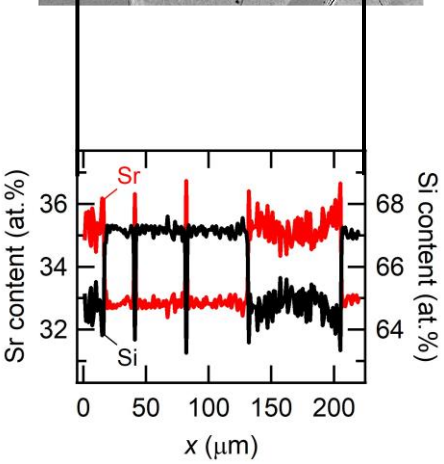

(e)

Fig. 3

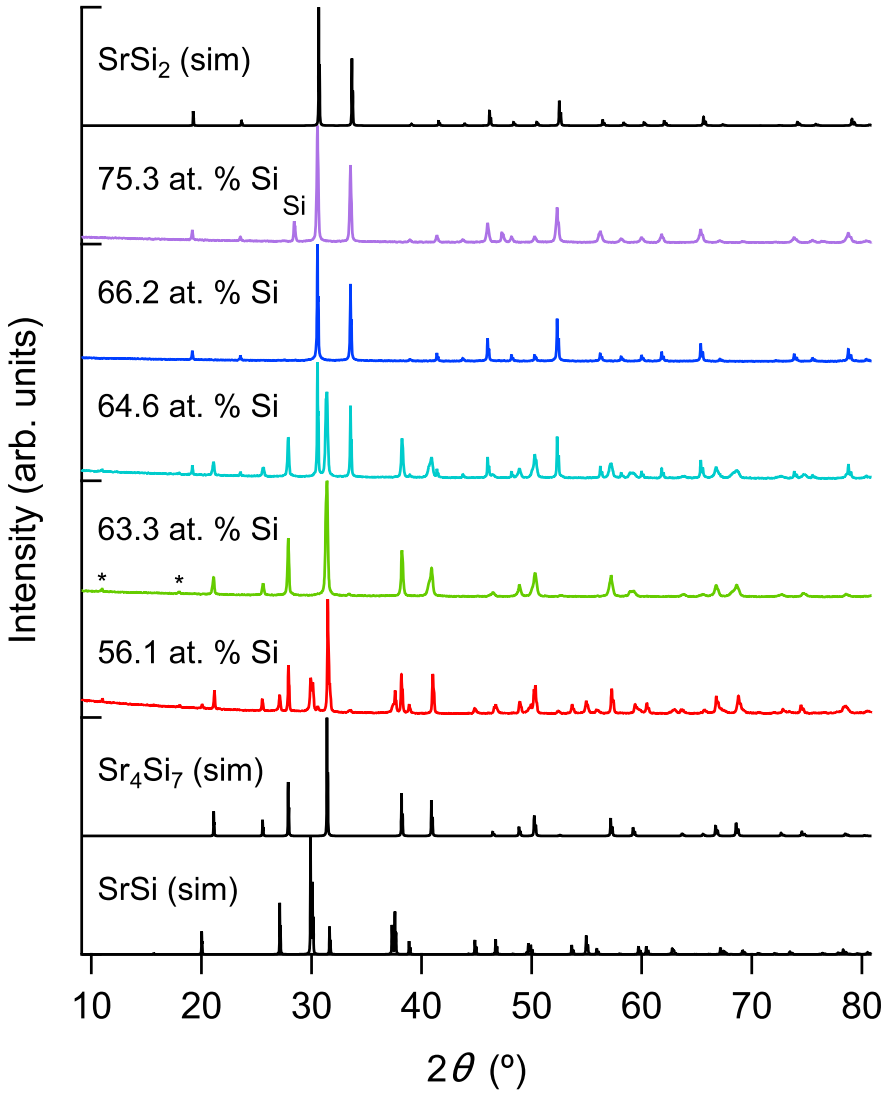
SrSi2 (sim)
75.3 at. % Si
Si
66.2 at. % Si
64.6 at. % Si
63.3 at. % Si
*
*
56.1 at. % Si
Sr4Si7 (sim)
SrSi (sim)
Intensity (arb. units)
10
20
30
40
50
60
70
80
2θ (°)

Fig. 4

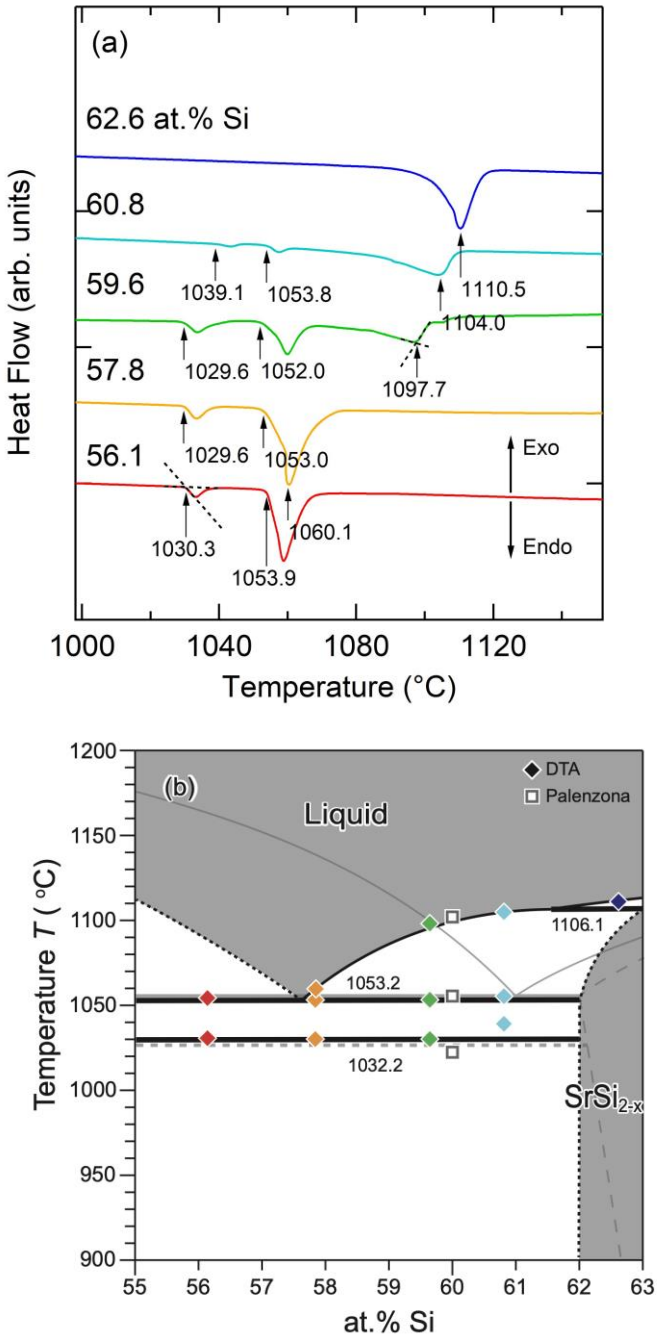
(a)
62.6 at.% Si
60.8
59.6
57.8
56.1
1039.1
1053.8
1110.5
1104.0
1029.6
1052.0
1097.7
1029.6
1053.0
1030.3
1053.9
1060.1
Exo
Endo
Heat Flow (arb. units)
1000
1040
1080
1120
Temperature (°C)
(b)
DTA
Palenzona
Liquid
1106.1
1053.2
1032.2
SrSi2-x
Temperature T (°C)
1200
1150
1100
1050
1000
950
900
55
56
57
58
59
60
61
62
63
at.% Si

Fig. 5

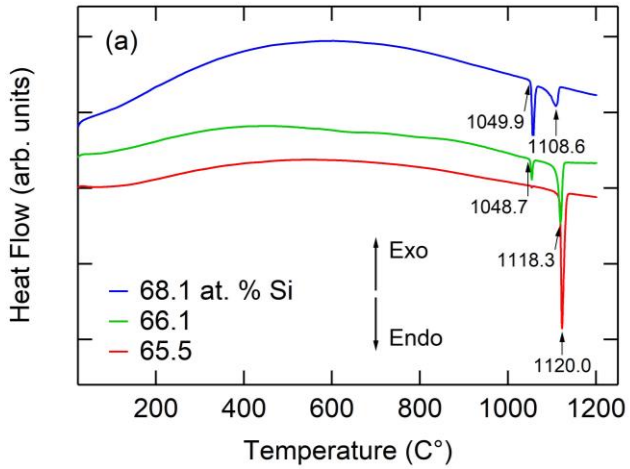
(a)
Heat Flow (arb. units)
1049.9
1108.6
1048.7
1118.3
1120.0
Exo
Endo
68.1 at. % Si
66.1
65.5
200
400
600
800
1000
1200
Temperature (C°)

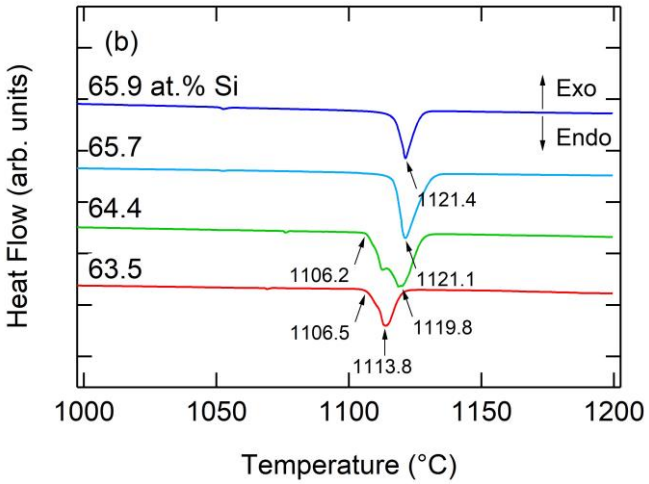
(b)
65.9 at.% Si
65.7
64.4
63.5
Exo
Endo
1121.4
1106.2
1121.1
1106.5
1119.8
1113.8
Heat Flow (arb. units)
1000
1050
1100
1150
1200
Temperature (°C)

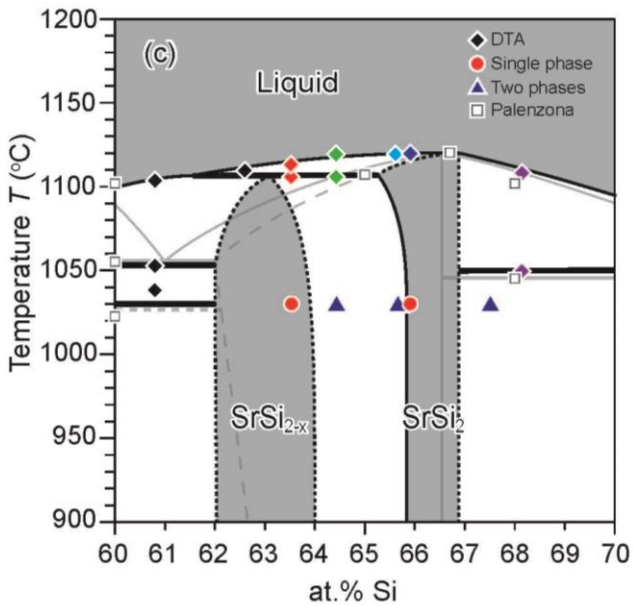
(c)
Liquid
DTA
Single phase
Two phases
Palenzona
SrSi2-x
SrSi2
Temperature T (°C)
1200
1150
1100
1050
1000
950
900
60
61
62
63
64
65
66
67
68
69
70
at.% Si

Fig. 6

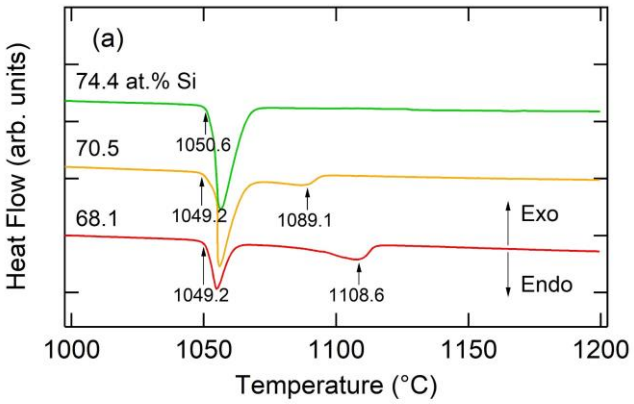
(a)
74.4 at.% Si
70.5
68.1
1050.6
1049.2
1089.1
1049.2
1108.6
Exo
Endo
Heat Flow (arb. units)
1000
1050
1100
1150
1200
Temperature (°C)

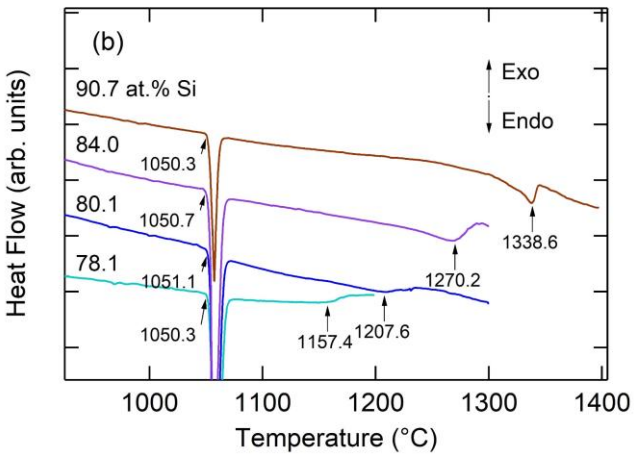
(b)
90.7 at.% Si
84.0
80.1
78.1
1050.3
1050.7
1051.1
1050.3
1157.4
1207.6
1270.2
1338.6
Exo
Endo
Heat Flow (arb. units)
1000
1100
1200
1300
1400
Temperature (°C)

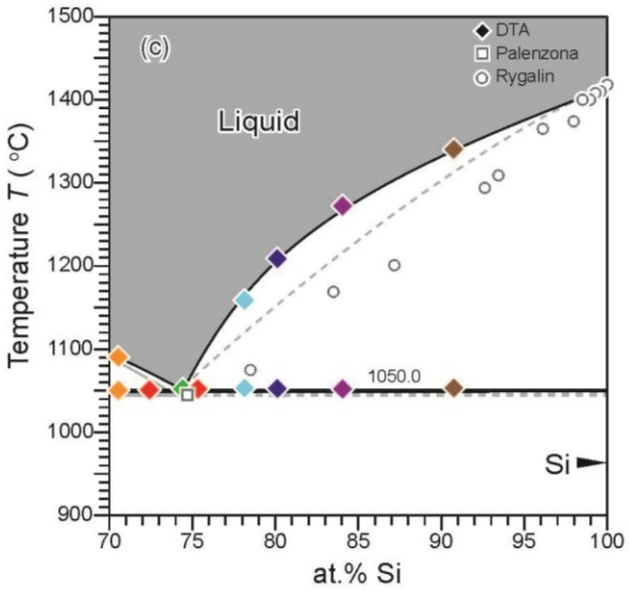
(c)
DTA
Palenzona
Rygalin
Liquid
1050.0
Si
Temperature T (°C)
1500
1400
1300
1200
1100
1000
900
70
75
80
85
90
95
100
at.% Si

Fig.7

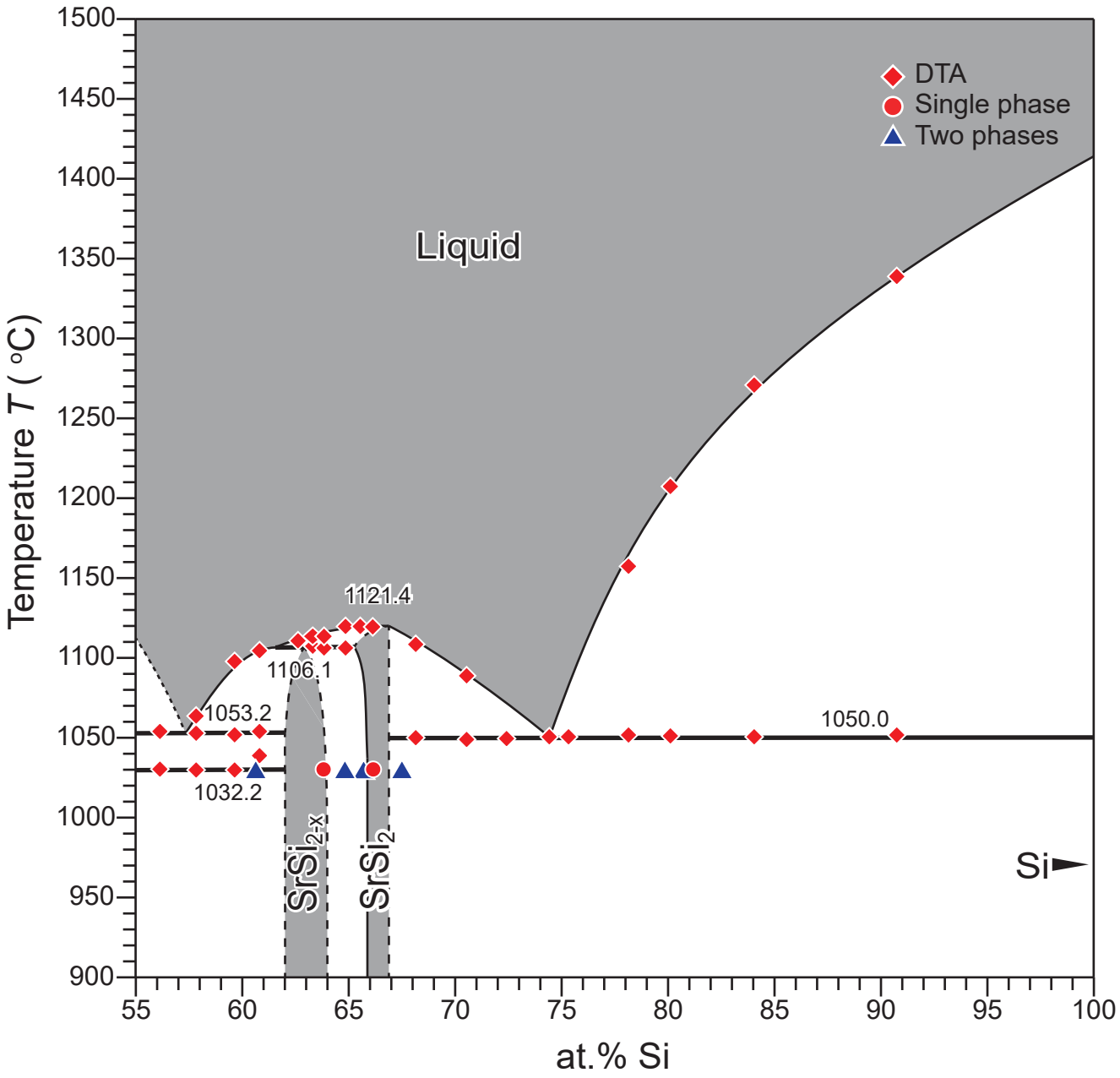
DTA
Single phase
Two phases
Liquid
1121.4
1106.1
1053.2
1050.0
1032.2
SrSi2-x
SrSi2
Si
Temperature T (°C)
at.% Si
1500
1450
1400
1350
1300
1250
1200
1150
1100
1050
1000
950
900
55
60
65
70
75
80
85
90
95
100

Fig. 8

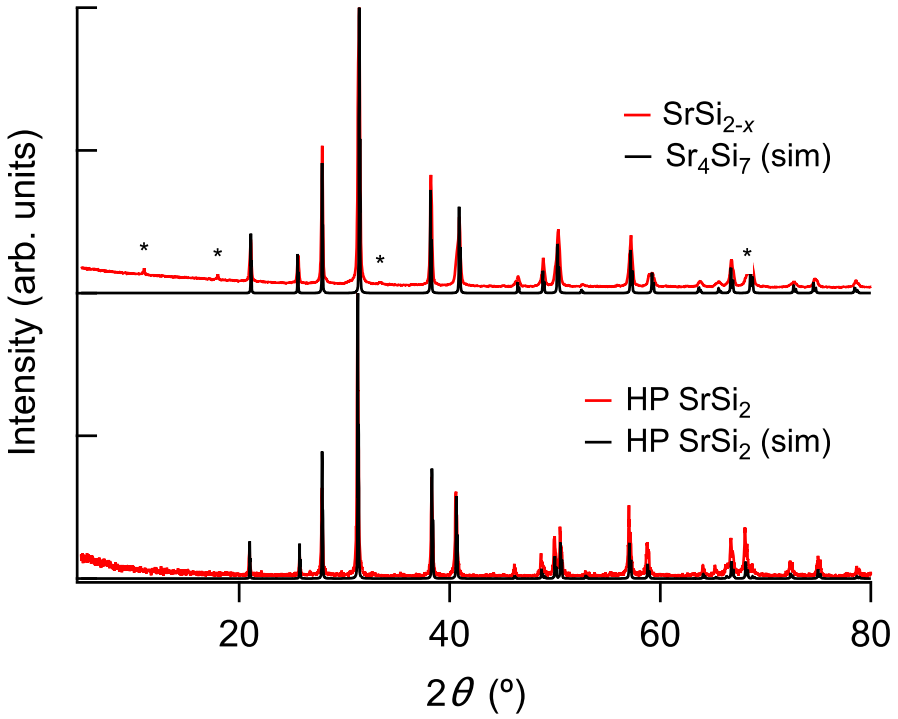
Intensity (arb. units)
SrSi2-x
Sr4Si7 (sim)
HP SrSi2
HP SrSi2 (sim)
*
*
*
*
20
40
60
80
2θ (°)

Fig. 9

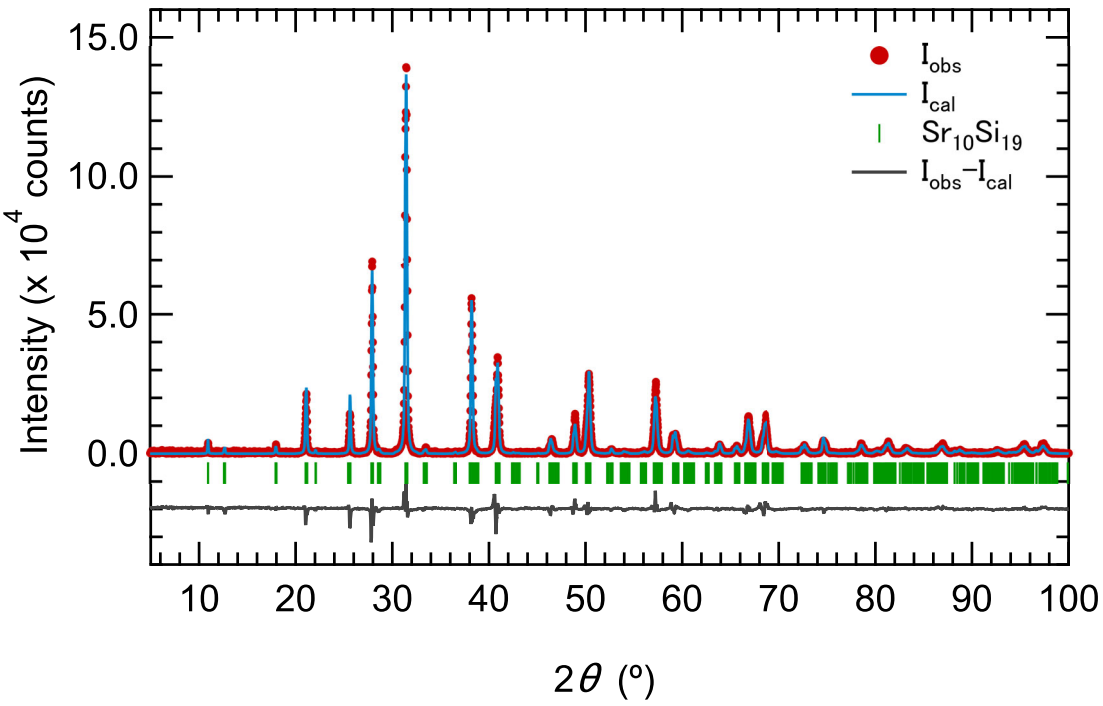
15.0
10.0
5.0
0.0
Intensity (x 10^4 counts)
10
20
30
40
50
60
70
80
90
100
2θ (°)
I_obs
I_cal
Sr10Si19
I_obs−I_cal

Fig. 10

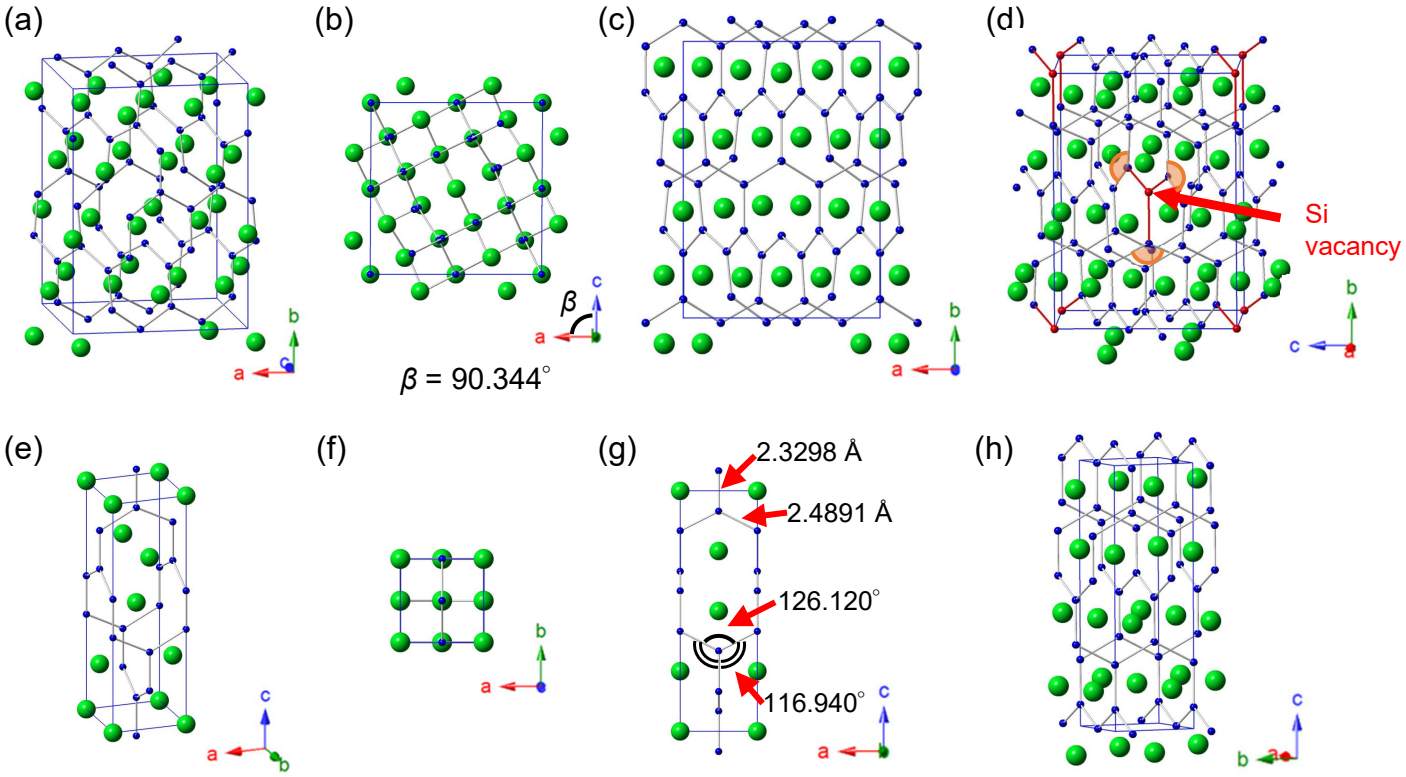

Fig. 11